



Facile two-step treatment of carbon nitride for preparation of highly efficient visible-light photocatalyst



Ningxin Jiang^{a,b}, Hongjia Wang^{a,b}, Yidan Luo^{a,b}, Shuohan Yu^{a,b}, Annai Liu^{a,b}, Weixin Zou^{a,b}, Fei Gao^{a,b,*}, Lin Dong^{a,b,*}

^a Jiangsu Key Laboratory of Vehicle Emissions Control, School of the Environment, Center of Modern Analysis, Nanjing 210093, PR China

^b Key Laboratory of Mesoscopic Chemistry of Ministry of Education, School of Chemistry and Chemical Engineering, Nanjing University, Nanjing 210093, PR China

ARTICLE INFO

Keywords:

Graphitic carbon nitride
Ammonia solution
Two-step treatment
Photocatalyst

ABSTRACT

Tailoring the microstructure of graphitic carbon nitride (GCN) is an effective way to improve its photocatalytic activities. Protonation of GCN has been extensively studied, while few researches focused on modifying GCN with alkali. Herein, we report a facile two-step hydrothermal-calcination method to modify GCN. After hydrothermal treatment with ammonia solution and subsequently calcination under argon atmosphere, the as-synthesized GCN-xh-Ar (x stands for hydrothermal time) samples exhibit drastically improved photocatalytic activities towards photocatalytic degradation of RhB and evolution of hydrogen. The GCN-2h-Ar sample shows the highest hydrogen evolution rate of $736 \mu\text{mol h}^{-1} \text{g}^{-1}$, which is nearly 11 times of pristine GCN ($67 \mu\text{mol h}^{-1} \text{g}^{-1}$). The improved activities of samples can be attributed to the higher surface area, larger pore volume and enhanced visible light absorption. This approach sheds light on the synthesis of highly efficient photocatalysts.

1. Introduction

Graphitic carbon nitride (GCN) is known as a metal-free polymer semiconductor which can be served as a catalyst for water splitting, pollutant photodegradation, CO₂ photoreduction and nitrogen fixation [1–5]. As a promising photocatalyst, it has several interesting properties including active in visible light region, stable and environmental friendly. However, the disadvantages of GCN are also conspicuous: the low surface area, low absorbance of visible light, and fast recombination of photogenerated electrons and holes [6]. Thus, numerous strategies have been employed to improve the efficiency of GCN such as nanoarchitecture design, functionalization of GCN, formation of proper heterostructures and loading with metal cocatalysts [7–12].

Various researches focused on the nanostructure design of GCN to tailor the interlayer relationship and structural properties of GCN. The band gap structure, surface area, porosity, morphology, structure and size of GCN can be easily modified with proper treatments and designs [10,13–15]. Most studies focused on one step treatment of GCN such as hydrothermal, protonation, calcination and sonication methods, which can easily tune some properties and thus improve the photocatalytic activities of carbon nitrides [16–26]. Hydrothermal method is an effective way to modify GCN. A lot of materials such as H₃PW₁₂O₄₀ [27], NiS [28], Bi₂WO₆ [29] and BiVO₄ [30] has been fabricate with carbon

nitride to build efficient heterojunction with hydrothermal methods. Hydrothermal treatment of pure carbon nitride in certain solution including water [16,17], sodium hydroxide [18] hydrogen peroxide solution [24] and the ammonia thiosulfate solution [25] is another way to get effective photocatalyst. However, few research use solution with high pH to modify the carbon nitride which might because the hydroxide ions will break the C–N–C bonds and decrease the polymerization degree of carbon nitride [18]. Thus, it is interesting to find a proper way of improving activities of carbon nitride with alkaline treatment.

Recently, some researchers focused on two-step methods which contain some of these one-step treatment to further improve the activities of GCN materials [23,31–39]. Typically, the first step aims at designing highly ordered nanoarchitecture by treating GCN or molecules rich in carbon and nitrogen such as melamine under hydrothermal conditions or heating in certain solutions. The second step is mostly calcination of GCN under different atmosphere to synthesis GCN with specific structure, higher polymerization degree and extended visible light absorption range. For example, the highly ordered layered porous GCN structures with higher activities towards photodegradation of RhB were prepared with an acetic acid induced two-step method [33]. Sulfuric acid can also be used as solvent in the first step and subsequent calcination of product can generate good photocatalysts [37,38]. However, it remains a challenge to synthesize GCN with proper two-

* Corresponding authors at: Jiangsu Key Laboratory of Vehicle Emissions Control, School of the Environment, Center of Modern Analysis, Nanjing 210093, PR China.
E-mail addresses: gaofei@nju.edu.cn (F. Gao), donglin@nju.edu.cn (L. Dong).

step treatment because most two-step methods use expensive and harmful reagents and the activities of catalysts are relatively low. Also, most methods employed acid in the first step while few research used basic solution in the first-step treatment. Thus, using alkaline treatment as the first step and calcinating the product under certain atmosphere might be a good way to obtain an active photocatalyst.

In this work, ammonia solution induced two-step hydrothermal-calcination method was developed for the preparation of highly efficient carbon nitride photocatalyst. After hydrothermal treatment of GCN in ammonia solution, the mixtures of melem hydrate hexagonal prisms and high-surface-area porous GCN are generated. The subsequent calcination process leads to the formation of GCN-xh-Ar (x stands for the hydrothermal time) composed of two types of carbon nitride. The two-step treatment provides the products with high surface area, large pore volume and effective visible-light harvesting ability. Thus, the as-synthesized product exhibits outstanding activities for photocatalytic production of H₂ and photodegradation of rhodamine B (RhB) under visible light irradiation.

2. Experimental sections

2.1. Preparation of catalytic materials

Bulk GCN was prepared by condensation of 10 g dicyandiamide in a crucible with a cover at 550 °C for 4 h with a ramping rate of 2.3 °C min⁻¹ in the air in a muffle furnace. The product was well grinded in an agate mortar and denoted as GCN-pure. Hydrothermal treatment in ammonia solution was performed as follows. 2.0 g GCN-pure and 25 mL saturated ammonia solution were mixed in a 50 mL Teflon-lined stainless-steel autoclave. The autoclave was heated at 150 °C for different time. The product was collected after the reaction and washed with deionized water several times and ethanol one time. The product was denoted as GCN-xh (x refers to different hydrothermal time) after drying in an oven at 100 °C for 12 h. 0.5 g GCN-xh was put into a porcelain boat. The boat was placed in the tube furnace and heated to 600 °C under argon with a ramping rate of 3 °C min⁻¹. The final product was denoted as GCN-xh-Ar. The sample directly calcinated under argon was designated as GCN-Ar. The synthesis process is illustrated in Fig. 1a.

2.2. Characterization

Powder X-ray diffraction (XRD) patterns were recorded on an XRD-6000 X-ray diffractometer (Shimadzu) using Ni-filtered Cu K α radiation ($\lambda = 0.15418 \text{ nm}$). Fourier transform infrared (FT-IR) spectra were collected on a Nicolet iS10 spectrometer. Scanning electron microscopy (SEM) experiments were performed on S-3400N II electron microscope. Transmission electron microscopy (TEM) images were taken on a JEM-

2100 instrument at an acceleration voltage of 200 kV. Brunauer-Emmet-Teller (BET) surface areas were measured by nitrogen adsorption at 77 K using an ASAP2020 physical adsorption instrument (Micromeritics). UV-vis diffuse reflectance spectroscopy (UV-vis DRS) were recorded by a Shimadzu UV-3600 spectrophotometer with BaSO₄ as reference. X-ray photoelectron spectra (XPS) analysis was performed on a PHI 5000 Versa Probe system with monochromatic Al K α radiation (1486.6 eV) operating at an accelerating power of 15 kW. The sample charging effects were compensated by calibrating all binding energies (BE) with the adventitious C 1s peak at 284.6 eV. Elemental analysis was performed on a CHN-O-Rapid instrument (Heraeus). The photoluminescence spectra and time-resolved photoluminescence emission spectra (335 nm excitation) were measured at room temperature with an FLsp-920 (Edinburgh) spectrophotometer.

2.3. Photocatalytic evaluation

The degradation of RhB was evaluated in aqueous solution under visible light irradiation. The visible light ($\lambda \geq 420 \text{ nm}$) was provided by 500 W metal halide lamp with a 420 nm cut-off filter. 50 mg catalyst was added to 50 mL RhB (10 mg L⁻¹) solution. Before irradiation, the suspension was stirred for 30 min in the dark to achieve the adsorption-desorption equilibrium between RhB and the catalysts. When the light was on, approximately 3 mL suspension was obtained from solution at fixed intervals (10 min) and removed catalysts after centrifugation. The concentration of RhB was analyzed by UV-vis spectrophotometer according to its absorbance at 554 nm.

The photocatalytic hydrogen generation reactions were carried out in a top-irradiation vessel connected to a gas-closed glass system under the irradiation of 300 W Xe lamp equipped with a 420 nm cut-off filter. Typically, 50 mg catalyst was dispersed in 100 mL aqueous solution containing 90 mL deionized water and 10 mL triethanolamine as electron donor. Proper amount of H₂PtCl₆ aqueous solution was added as the precursor of Pt which was in-situ reduced during the reaction (3 wt % Pt). The temperature of solution was maintained at 6 °C during the experiment. The reactor was sealed and evacuated for 30 min before reaction. The amount of hydrogen gas was determined by a gas chromatograph.

3. Result and discussion

3.1. Morphology and structural characterization

The structures of as-obtained GCN-xh and GCN-xh-Ar were verified by X-ray diffraction (XRD, Fig. 2a) and Fourier transform infrared (FT-IR, Fig. 2b). The XRD patterns of GCN-xh show both melem hydrate and GCN diffraction peaks which indicate the formation melem hydrate in samples after hydrothermal treatment [40]. The FT-IR spectra of

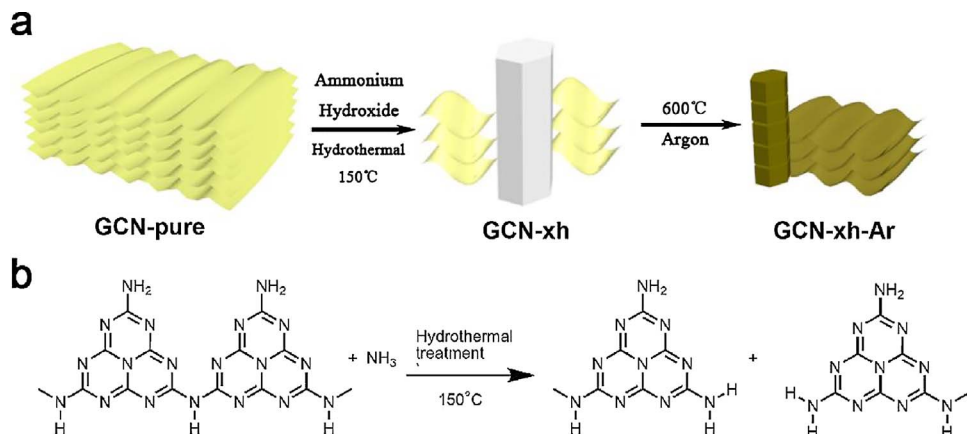


Fig. 1. a) Schematic model of formation of GCN-xh-Ar. b) Reaction scheme of aminolysis of GCN.

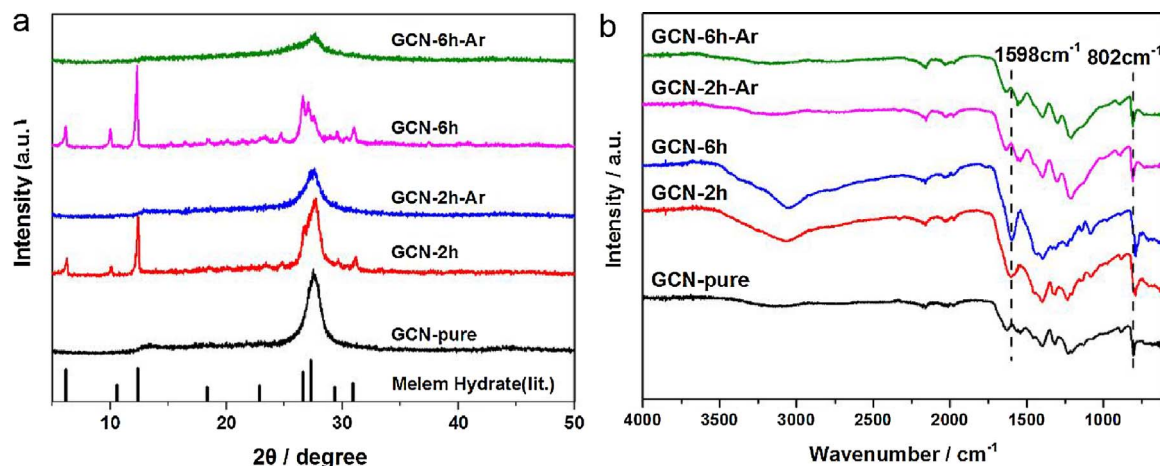


Fig. 2. a) XRD patterns and b) FT-IR spectra of GCN-pure, GCN-xh and GCN-xh-Ar.

GCN-2h and GCN-6h also prove the formation of melem hydrate with the increasing absorption bands at 1598 cm^{-1} which is the characteristic absorption peaks of melem species [41]. The GCN-xh-Ar samples show peaks only at 13.1° and 27.2° which suggests that the melem hydrates change into GCN after calcination. Notably, The 13.1° peak which associated with hydrogen bonds maintaining interlayer long-range atomic order between tri-s-triazine units almost disappears for GCN-xh-Ar samples indicate the breaking of hydrogen bonds after heating [19]. On the other hand, the intensity of 27.2° peak for GCN-xh-Ar decrease obviously which shows the lower crystallinity of GCN after two-step treatment [36]. The similarity of FT-IR spectra between GCN-xh-Ar and GCN-pure further proves the formation of GCN after calcination. All samples show intense absorption band at around 802 cm^{-1} , which is the absorption band of triazine units in melem hydrate and carbon nitride [42].

The stoichiometry, chemical states and polymerization degree of samples were revealed by X-ray photoelectron spectroscopy (XPS, Fig. 3a, b) and elemental analysis. The GCN-pure, GCN-2h-Ar and GCN-6h-Ar show the similar C1s spectra (Fig. 3a). The C1s spectra are resolved into two peaks centered at 287.7 eV and 284.6 eV , which can be assigned to the C species in $\text{N}-\text{C}=\text{N}$ bonds and the $\text{C}-\text{C}$ bonds respectively in GCN-pure sample [43]. The N1s spectra (Fig. 3b) can be fitted to three peaks with binding energies at 398.2 eV , 399.4 eV , and 400.7 eV , which can be assigned to nitrogen species in $\text{N}(\text{C})_2$, $\text{N}(\text{C})_3$, and $\text{N}(\text{CH})$ groups of GCN respectively in GCN-pure sample [37]. Both peaks of C1s and N1s show small variations due to the change of microstructure and atomic ratio after two-step treatment. The peak area

Table 1

Summary of BET surface area, pore volume and atomic ratio of carbon to nitrogen in GCN-pure, GCN-xh and GCN-xh-Ar.

Samples	C/N atomic ratio	Surface area($\text{m}^2\text{ g}^{-1}$)	Pore volume($\text{cm}^3\text{ g}^{-1}$)
GCN-pure	3:4.52	14.4	0.041
GCN-2h	3:4.73	55.0	0.196
GCN-2h-Ar	3:4.26	37.6	0.212
GCN-6h	3:4.88	22.7	0.089
GCN-6h-Ar	3:4.26	31.4	0.063

ratio of $\text{N}(\text{C})_3$ to $\text{N}(\text{C})_2$ in GCN-pure, GCN-2h-Ar and GCN-6h-Ar are 0.28, 0.70 and 0.70 respectively, which shows the improvement of polymerization degree for calcinated samples. The increased polymerization degree can also be supported by elemental analysis (Table 1). The C/N atomic ratio for GCN-2h and GCN-6h is closer to 3:5 due to the melem hydrate content. The C/N atomic ratios are closer to 3:4 of stoichiometric C_3N_4 for GCN-2h-Ar and GCN-6h-Ar in comparison to GCN-pure. It is known that higher C/N atomic ratio of GCN indicates higher polymerization degree [19]. The higher polymerization degree in the calcinated samples arise from the loss of amino groups in samples after calcination and can improve the transportation of electrons in catalysts [44,45].

The morphologies of the obtained samples were studied by scanning electron microscope (SEM) and transmission electron microscope (TEM). As shown in Fig. 4a, the GCN-pure sample is mainly composed of irregular particles with $10\text{--}40\text{ }\mu\text{m}$ in diameter. Smaller irregular particles in GCN-2h samples (Fig. 4b) with $5\text{ }\mu\text{m}$ in diameter show that

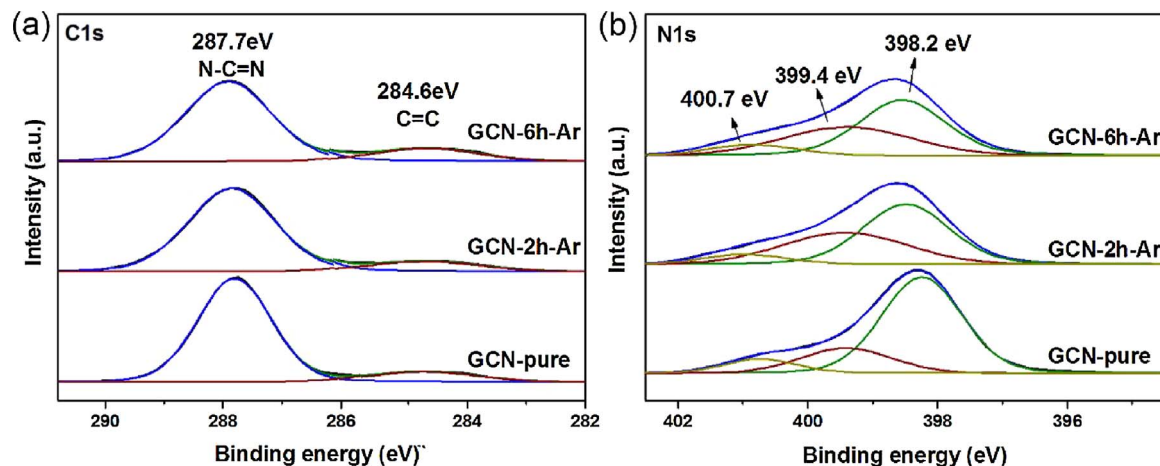


Fig. 3. High-resolution XPS (a) C1s spectra; b) N1s spectra of GCN-pure, GCN-2h-Ar and GCN-6h-Ar.

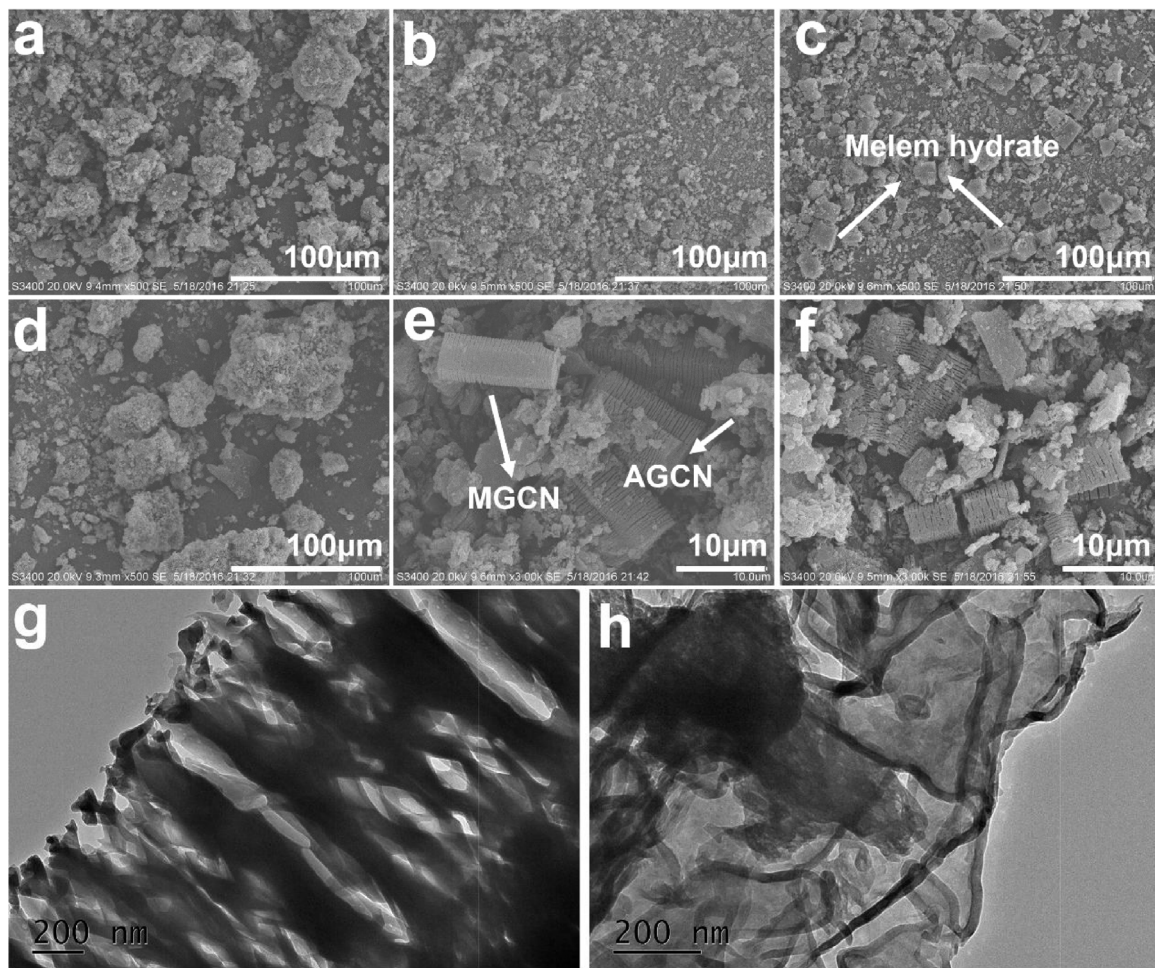


Fig. 4. SEM images of (a) GCN-pure, (b) GCN-2h, (c) GCN-6h, (d) GCN-Ar, (e) GCN-2h-Ar, (f) GCN-6h-Ar. TEM images of (g) MGCN and (h) AGCN in GCN-2h-Ar.

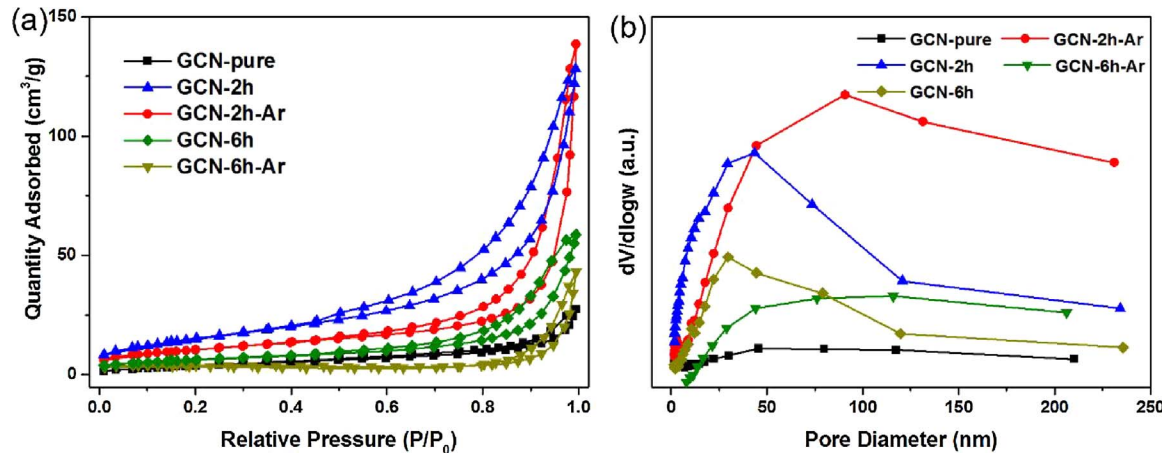


Fig. 5. N_2 adsorption-desorption isotherms and b) Pore distribution curves of samples.

the hydrothermal treatment can drastically reduce the size of particles. The formation of hexagonal prism with 15 μm in length can also be observed in GCN-2h (Fig. S1). More prisms which are larger in size appear in GCN-6h samples (Fig. 4c, Fig. S2). Combined with the intensified melem hydrate peaks in the XRD patterns of GCN-6h, we can draw the conclusion that the hexagonal prism in hydrothermal treated samples are melem hydrates.

For GCN-2h-Ar (Fig. 4e), particles with 20 μm in diameter and laminated hexagonal prisms with 10 μm in length are observed. Based on the SEM images of GCN-xh, these irregular particles can be ascribed to

the aggregation of smaller GCN particles in GCN-xh which are denoted as aggregated graphitic carbon nitride (AGCN). The laminated hexagonal prisms came from the condensation of melem hydrates which are designated as melem-derived graphitic carbon nitride (MGCN). TEM are used to further study two species in GCN-2h-Ar. The MGCN shown in Fig. 4g is layered structure composed of nanosheets with large cracks on the surface of nanosheets. Such laminated porous structure of GCN has been reported before and shows low crystalline property as well which is in accord with the XRD patterns of GCN-xh-Ar [33]. This result indicates that the calcination procedure introduced mesopores

into GCN in GCN-xh samples. The AGCN showed in Fig. 4h exhibits ultrathin layered structures with mesopores on the surface. These AGCN particles have the similar size as the particles in GCN-Ar sample (Fig. 4d) which also shows that they are formed by the aggregation of smaller GCN particles.

The N₂ adsorption-desorption measurements are used to study the pore structure and BET surface area of samples. As shown in Table 1, both GCN-xh and GCN-xh-Ar samples show higher surface area and larger pore volume compared with GCN-pure. The N₂ adsorption-desorption isotherm of all samples (Fig. 5a) are typically type III with a H3 hysteresis loop at $0.45 < P_0 < 1.0$, which can be attributed to the opened mesoporous structure formed by the assembly of nanosheets [37]. The pore size distributions of samples (Fig. 5b) changed after calcination. The GCN-xh and GCN-xh-Ar sample show broad pore distribution ranged from 50 to 200 nm. However, the calcination step created abundant pores with size in 100–200 nm for both GCN-2h-Ar and GCN-6h-Ar samples. These large pores can be attributed to the large cracks shown in Fig. 4g.

Therefore, we can conclude that GCN-xh samples composed of smaller GCN particles and melem hydrates hexagonal prisms. The C–N–C bonds between two melem units break down slowly during the whole hydrothermal process (shown in Fig. 1b). This reaction decomposes the unstable domains of GCN at the beginning of reaction [18]. As time goes on, the completely destruction of the C–N–C bonds between melem units induces the formation of melem hydrates [17]. After calcination, the samples become GCN with lower crystallinity and higher polymerization degree consist of MGCN and AGCN. The MGCN with abundant mesopores is formed due to the thermal condensation of melem hydrate and these mesopores might induce the decreasing of crystallinity. At the same time, the GCN in GCN-xh aggregate into AGCN.

3.2. Optical and photophysical properties

UV-vis absorption spectra were employed to study the optical properties of samples. An obvious red-shifted optical absorption edge is observed in UV-vis absorption spectra (Fig. 6a) for both GCN-2h-Ar and GCN-6h-Ar. At the same time, weak intrinsic absorption bands starting from 460 nm to 650 nm formed for calcinated samples. These changes can be explained by the result of the changed microstructure of GCN products with broken hydrogen bonds [19]. The band gaps of samples are shown in Table S1 based on the Kubelka-Munk function plot (Fig. 4a). The band gaps of samples (Table 2) decrease gradually from 2.72 eV for GCN-pure to 2.44 eV for GCN-6h-Ar.

To reveal the photophysical characteristics of photogenerated charge carriers, the time-resolved photoluminescence spectra (Fig. S3) are carried out. The fluorescence intensities of samples decay

Table 2

Summary of band gaps and average fluorescence lifetime in GCN-pure, GCN-Ar and GCN-xh-Ar.

Sample	Band gap (eV)	Average lifetime (ns)
GCN-pure	2.76	9.38
GCN-2h-Ar	2.62	7.38
GCN-6h-Ar	2.44	6.57

exponentially. The calculated average lifetime values are shown in Table 2. Both GCN-2h-Ar and GCN-6h-Ar exhibit shorter average lifetime values in comparison to GCN-pure which is due to the band-tails-involved rapid radiative electron-hole combination process [19]. However, the GCN-2h-Ar sample has a longer lifetime value than GCN-6h-Ar which might due to the proper ratio of MGCN to AGCN. The isotype heterojunction between MGCN and AGCN could facilitate the charge carrier transfer and suppress the radiative recombination and thus improve the fluorescence lifetime value [31,46,47].

3.3. Photocatalytic activities of samples and possible mechanisms

The photocatalytic degradation of rhodamine B (RhB) was investigated to reveal the photocatalytic activity of GCN-pure, GCN-Ar and GCN-xh-Ar under visible light irradiation ($\lambda \geq 420$ nm, Fig. 7a). Compared with GCN-pure, the calcinated samples have improved photodegradation activities. For 50 min, GCN-2h-Ar could mostly decompose RhB while only 47% RhB was degraded by GCN-pure. The rate constant (k) value of GCN-2h-Ar is 0.0612 min^{-1} , which is 4.5 and 3.8 times higher than that of GCN-pure and GCN-Ar, respectively.

The photocatalytic hydrogen evolution of as-prepared samples was measured from an aqueous solution containing triethanolamine (TEOA) with Pt (3 wt%) as cocatalyst under visible light irradiation ($\lambda \geq 420$ nm) and are shown in Fig. 7b. The calcinated samples exhibit a much higher activity to GCN-pure. The GCN-2h-Ar shows the peak activity among samples. The hydrogen generation rate of GCN-2h-Ar is $736 \mu\text{mol h}^{-1} \text{ g}^{-1}$, which is much higher than that of GCN-pure ($67 \mu\text{mol h}^{-1} \text{ g}^{-1}$) and GCN-Ar ($228 \mu\text{mol h}^{-1} \text{ g}^{-1}$). After the normalization of hydrogen evolution rate by surface area, the GCN-2h-Ar still shows higher activity than other samples which proves that the two-step method improve the catalytic activity of each active sites (Table S1 in SI). The GCN-2h-Ar in this work also shows better performance than those GCN based catalysts with similar structure (Table S2 in SI). To confirm the stability of H₂ evolution by GCN-2h-Ar, the photocatalytic reaction was tested for 25 h (Fig. 7c). The system was evacuated every 5 h under visible light irradiation. The H₂ evolution rate was stable for two cycles and decreased slightly after the third cycles. However, after adding TEOA, the H₂ evolution rate recovered and remained stable for

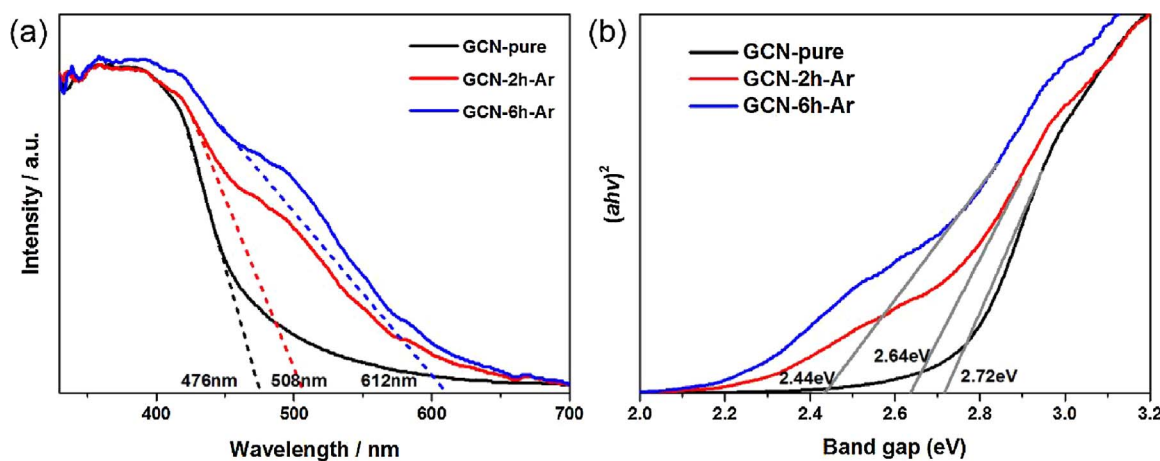


Fig. 6. a) UV-vis absorption spectra and b) plots of $(ahv)^2$ versus energy ($h\nu$) of GCN-pure and GCN-xh-Ar.

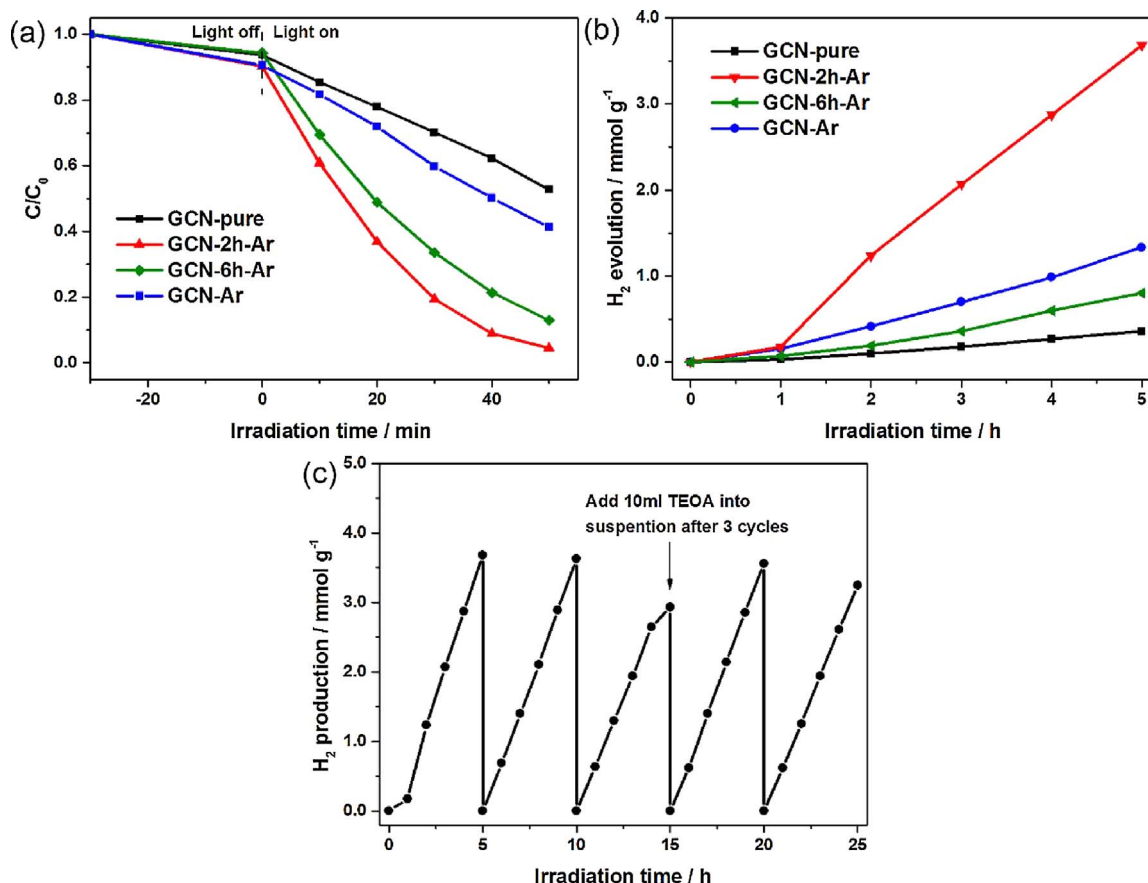


Fig. 7. a) Photocatalytic degradation of RhB and b) photocatalytic activity for H₂ evolution of GCN-pure, GCN-Ar and GCN-xh-Ar under visible light ($\lambda \geq 420$ nm) irradiation; c) photocatalytic H₂ evolution stability test on GCN-2h-Ar under visible light.

another cycle. This result indicates the good photocatalytic stability of H₂ evolution reaction for GCN-2h-Ar.

The photocatalysts experience three steps during photocatalytic reactions including (i) absorption of photon, (ii) charge separation and (iii) transfer of charge carriers on surface [48]. The drastically enhanced activity of GCN-xh-Ar can be attributed to the successful modification of these three steps. First, the two-step treatment provides samples with the higher BET surfaces area, less hydrogen bonds and a large amount of mesopores which offered photocatalysts with abundant active catalytic sites and channels for photocatalytic reaction [49,50]. Second, the calcination step extends visible light absorption range for GCN-xh-Ar which induces the absorption of low-energy photon and thus generates more electron-hole pairs. Moreover, the heterostructure between MGCN and AGCN in GCN-2h-Ar suppressed the radiative electron-hole recombination and exhibits the longer fluorescence lifetime compare to GCN-6h-Ar. Although the GCN-pure has a longer fluorescence lifetime value, the GCN-2h-Ar with high BET surface area, large pore volume and wide visible light absorption range shows highest photocatalytic activities toward degradation of RhB and evolution of hydrogen.

4. Conclusion

In summary, highly efficient visible-light photocatalyst was synthesized through a two-step treatment of bulk GCN. GCN-xh composed of small porous GCN particles and melem hydrate hexagonal prisms was formed after hydrothermal treatment of GCN-pure. Subsequently, GCN-xh-Ar contains melem derived GCN and aggregated GCN was generated after heating GCN-xh under argon atmosphere. Compared to GCN-pure, the GCN-xh-Ar exhibits enhanced activities for photocatalytic degradation of RhB and hydrogen evolution reaction under visible light.

The GCN-2h-Ar sample shows the highest hydrogen evolution rate of $736 \mu\text{mol h}^{-1} \text{g}^{-1}$, which is nearly 11 times of GCN-pure ($67 \mu\text{mol h}^{-1} \text{g}^{-1}$). The drastically enhanced activities can be attributed to the synergistic effects between higher BET surface area, larger pore volume and improved optical absorption of samples. This facile two-step method provides a novel way for the synthesis of carbon nitride based photocatalysts with specific microstructure and enhanced photocatalytic activities.

Acknowledgements

The financial supports of the National Natural Science Foundation of China (No. 21573105) and Natural Science Foundation of Jiangsu Province (BK20161392) are gratefully acknowledged.

Appendix A. Supplementary data

Supplementary data associated with this article can be found, in the online version, at <https://doi.org/10.1016/j.apcatb.2018.01.056>.

References

- [1] X. Wang, K. Maeda, A. Thomas, K. Takanabe, G. Xin, J.M. Carlsson, K. Domen, M. Antonietti, Nat. Mater. 8 (2009) 76–80.
- [2] D.J. Martin, P.J.T. Reardon, S.J. Moniz, J. Tang, J. Am. Chem. Soc. 136 (2014) 12568–12571.
- [3] L. Shi, T. Wang, H. Zhang, K. Chang, J. Ye, Adv. Funct. Mater. 25 (2015) 5360–5367.
- [4] G. Dong, W. Ho, C. Wang, J. Mater. Chem. A 3 (2015) 23435–23441.
- [5] J. Qin, S. Wang, H. Ren, Y. Hou, X. Wang, Appl. Catal. B Environ. 179 (2015) 1–8.
- [6] Y. Zheng, L. Lin, B. Wang, X. Wang, Angew. Chem. Int. Ed. 54 (2015) 12868–12884.
- [7] W.-J. Ong, L.-L. Tan, Y.H. Ng, S.-T. Yong, S.-P. Chai, Chem. Rev. 116 (2016) 7159–7329.

- [8] J. Liu, H. Wang, Z.P. Chen, H. Moehwald, S. Fiechter, R. van de Krol, L. Wen, L. Jiang, M. Antonietti, *Adv. Mater.* 27 (2015) 712–718.
- [9] X. Wang, X. Chen, A. Thomas, X. Fu, M. Antonietti, *Adv. Mater.* 21 (2009) 1609–1612.
- [10] H. Wang, L. Zhang, Z. Chen, J. Hu, S. Li, Z. Wang, J. Liu, X. Wang, *Chem. Soc. Rev.* 43 (2014) 5234–5244.
- [11] Y. Yang, Y. Guo, F. Liu, X. Yuan, Y. Guo, S. Zhang, W. Guo, M. Huo, *Appl. Catal. B Environ.* 142 (2013) 828–837.
- [12] K. Li, Z. Zeng, L. Yan, S. Luo, X. Luo, M. Huo, Y. Guo, *Appl. Catal. B Environ.* 165 (2015) 428–437.
- [13] H. Yan, *Chem. Commun.* 48 (2012) 3430–3432.
- [14] Z. Yang, Y. Zhang, Z. Schnepp, *J. Mater. Chem. A* 3 (2015) 14081–14092.
- [15] Z. Tong, D. Yang, Z. Li, Y. Nan, F. Ding, Y. Shen, Z. Jiang, *ACS Nano* 11 (2017) 1103–1112.
- [16] L. Ming, H. Yue, L. Xu, F. Chen, *J. Mater. Chem. A* 2 (2014) 19145–19149.
- [17] S. Liu, H. Sun, K. O'Donnell, H. Ang, M.O. Tade, S. Wang, *J. Colloid Interface Sci.* 464 (2016) 10–17.
- [18] T. Sano, S. Tsutsui, K. Koike, T. Hirakawa, Y. Teramoto, N. Negishi, K. Takeuchi, *J. Mater. Chem. A* 1 (2013) 6489–6496.
- [19] Y. Kang, Y. Yang, L.C. Yin, X. Kang, L. Wang, G. Liu, H.M. Cheng, *Adv. Mater.* 28 (2016) 6471–6477.
- [20] Y. Kang, Y. Yang, L.C. Yin, X. Kang, G. Liu, H.M. Cheng, *Adv. Mater.* 27 (2015) 4572–4577.
- [21] P. Qiu, H. Chen, C. Xu, N. Zhou, F. Jiang, X. Wang, Y. Fu, *J. Mater. Chem. A* 3 (2015) 24237–24244.
- [22] X. Bai, S. Yan, J. Wang, L. Wang, W. Jiang, S. Wu, C. Sun, Y. Zhu, *J. Mater. Chem. A* 2 (2014) 17521–17529.
- [23] J. Li, X. Zhang, F. Raziq, J. Wang, C. Liu, Y. Liu, J. Sun, R. Yan, B. Qu, C. Qin, L. Jing, *Appl. Catal. B Environ.* 218 (2017) 60–67.
- [24] G. Dong, Z. Ai, L. Zhang, *RSC Adv.* 4 (2014) 5553–5560.
- [25] Z. Hong, B. Shen, Y. Chen, B. Lin, B. Gao, *J. Mater. Chem. A* 1 (2013) 11754–11761.
- [26] X. Song, Q. Yang, X. Jiang, M. Yin, L. Zhou, *Appl. Catal. B Environ.* 217 (2017) 322–330.
- [27] K. Li, L. Yan, Z. Zeng, S. Luo, X. Luo, X. Liu, H. Guo, Y. Guo, *Appl. Catal. B Environ.* 156 (2014) 141–152.
- [28] J. Hong, Y. Wang, Y. Wang, W. Zhang, R. Xu, *ChemSusChem* 6 (2013) 2263–2268.
- [29] Y. Tian, B. Chang, J. Lu, J. Fu, F. Xi, X. Dong, *ACS Appl. Mater. Interfaces* 5 (2013) 7079–7085.
- [30] Y. Tian, B. Chang, Z. Yang, B. Zhou, F. Xi, X. Dong, *RSC Adv.* 4 (2014) 4187–4193.
- [31] Z. Tong, D. Yang, Y. Sun, Y. Nan, Z. Jiang, *Small* 12 (2016) 4093–4101.
- [32] X. Yuan, C. Zhou, Y. Jin, Q. Jing, Y. Yang, X. Shen, Q. Tang, Y. Mu, A.-K. Du, *J. Colloid Interface Sci.* 468 (2016) 211–219.
- [33] H. Fan, N. Wang, Y. Tian, S. Ai, J. Zhan, *Carbon* 107 (2016) 747–753.
- [34] W. Xing, G. Chen, C. Li, J. Sun, Z. Han, Y. Zhou, Y. Hu, Q. Meng, *ChemCatChem* 8 (2016) 2838–2845.
- [35] Q. Gu, Y. Liao, L. Yin, J. Long, X. Wang, C. Xue, *Appl. Catal. B Environ.* 165 (2015) 503–510.
- [36] J. Wang, Y. Shen, Y. Li, S. Liu, Y. Zhang, *Chem. Eur. J.* 22 (2016) 12449–12454.
- [37] Z. Huang, F. Li, B. Chen, G. Yuan, *ChemSusChem* 9 (2016) 478–484.
- [38] H. Yan, Y. Chen, S. Xu, *Int. J. Hydrogen Energy* 37 (2012) 125–133.
- [39] J. Zhang, M. Zhang, R.Q. Sun, X. Wang, *Angew. Chem.* 124 (2012) 10292–10296.
- [40] S.J. Makowski, P. Köstler, W. Schnick, *Chem. Eur. J.* 18 (2012) 3248–3257.
- [41] S. Chu, C. Wang, J. Feng, Y. Wang, Z. Zou, *Int. J. Hydrogen Energy* 39 (2014) 13519–13526.
- [42] B. Jürgens, E. Irran, J. Senker, P. Kroll, H. Müller, W. Schnick, *J. Am. Chem. Soc.* 125 (2003) 10288–10300.
- [43] L. Shi, K. Chang, H. Zhang, X. Hai, L. Yang, T. Wang, J. Ye, *Small* 12 (2016) 4431–4439.
- [44] A. Shi, H. Li, S. Yin, B. Liu, J. Zhang, Y. Wang, *Appl. Catal. B Environ.* 218 (2017) 137–146.
- [45] V.W.-h. Lau, I. Moudrakovski, T. Botari, S. Weinberger, M.B. Mesch, V. Duppel, J. Senker, V. Blum, B.V. Lotsch, *Nat. Commun.* 7 (2016) 12165.
- [46] F. Dong, Z. Zhao, T. Xiong, Z. Ni, W. Zhang, Y. Sun, W.-K. Ho, *ACS Appl. Mater. Interfaces* 5 (2013) 11392–11401.
- [47] X. Yang, F. Qian, G. Zou, M. Li, J. Lu, Y. Li, M. Bao, *Appl. Catal. B Environ.* 193 (2016) 22–35.
- [48] H. Tong, S. Ouyang, Y. Bi, N. Umezawa, M. Oshikiri, J. Ye, *Adv. Mater.* 24 (2012) 229–251.
- [49] H. Lan, L. Li, X. An, F. Liu, C. Chen, H. Liu, J. Qu, *Appl. Catal. B Environ.* 204 (2017) 49–57.
- [50] K.S. Lakhi, D.-H. Park, K. Al-Bahily, W. Cha, B. Viswanathan, J.-H. Choy, A. Vinu, *Chem. Soc. Rev.* 46 (2017) 72–101.